ARTICLES
https://doi.org/10.1038/s41929-021-00715-w

nature catalysis

Valence oscillation and dynamic active sites in monolayer NiCo hydroxides for water oxidation

Jianxin Kang[1,8], Xiaoyi Qiu[1,8], Qi Hu[2,3,8], Jun Zhong[4], Xiang Gao[5], Rong Huang[6], Chengzhang Wan[7], Li-Min Liu[3]✉, Xiangfeng Duan[7] and Lin Guo[1]✉

Monolayer materials are endowed with an additional degree of freedom to modulate electronic structures and catalytic performances. Here, we report a direct synthesis of monolayer $Ni(OH)_2$ on electrodes by in situ electrochemical conversion and a fundamental investigation of their catalytic activity. The monolayer structure greatly promotes hydrogen and oxygen release processes to produce dynamic active sites for the oxygen evolution reaction (OER) at a lower potential. Lattice doping with cobalt further tunes the electronic structure to reduce the overpotential. In situ experiments revealed Ni and Co valence state oscillation in NiCo hydroxides, which has been attributed to sequential dehydrogenation and deoxygenation processes, and fundamentally contributes to the dynamic generation of OER active sites. This study defines an in situ conversion process to yield monolayer layered double hydroxides (LDHs) and establishes a critical fundamental understanding of the origin of the active sites in monolayer LDHs for the OER.

Without the constraints of a bulk lattice, monolayer nanosheets could provide an additional degree of freedom to tailor their atomic structures, electronic structures and thus their catalytic properties[1–6]. For example, the layer-number-dependent electronic properties of layered transition metal dichalcogenides have attracted intense interest in fundamental studies and for a new generation of atomically thin electronic and optoelectronic devices[7–9]. Layered double hydroxides (LDHs) represent tunable catalysts, especially for the oxygen evolution reaction (OER)[10–12]. The OER plays a key role in diverse electrochemical energy conversion processes, such as water splitting, fuel cells and metal–air batteries[13,14]. A variety of OER catalysts, from noble metal oxides to first-row 3*d* transition metal LDHs, perovskites and polyoxometalates, have been explored to tackle the sluggish kinetics of the four-electron transfer process[15–18]. The activity of the OER has been suggested to be highly dependent on the high valence state of metal sites, arising from the preceding dehydrogenation process[19,20]. Additionally, lattice oxygen atoms also play a critical role in the OER during bond-breaking/formation processes[21–23]. An atomistic understanding of the hydrogen and oxygen release processes is a fundamental prerequisite for OER activity, but it remains a persistent challenge to identify the generation and evolution of active sites from both experimental and theoretical perspectives, due to the complicated atom- and charge-transfer processes in typical LDHs.

The OER is mainly limited to the near-surface region of a catalyst[24], and an in-depth understanding of the roles of surface metallic sites and lattice oxygen atoms is essential for the rational design of high-performance OER catalysts. In this regard, monolayer LDH nanosheets represent an attractive platform for exploring correlations between atomic environment, electronic structure and intrinsic electrocatalytic properties. Although considerable progress has been made in producing monolayer materials[25–28], the true activity of the monolayer on an electrode is difficult to achieve because of the restacking of monolayer LDHs during preserving or loading on the electrode. Monolayer inorganic hydroxides dispersed in solution are generally highly prone to aggregation or restacking and require highly polar solvents or excessive surfactants to ensure a stable dispersion of the monolayer material[29–32], which would inevitably block the surface sites for catalytic reactions. Additionally, it is also generally difficult to prevent the as-prepared nanosheets from restacking to form multilayers when loading them onto an electrode for electrochemical reactions[33,34].

Here, we report the direct preparation of monolayer amorphous $Ni(OH)_2$ on electrodes through an in situ electrochemical conversion of monolayer nickel acetylacetonate ($Ni(acac)_2$) molecular crystals. By avoiding the sluggish diffusion of atoms in their multilayer counterparts, the formation of monolayer materials readily facilitates the dehydrogenation process and subsequent oxygen release in $Ni(OH)_2$ to produce the oxygen vacancies (O_v) that are critical for the OER process. The introduction of Co dopants further tunes the electronic structure of the monolayer material to promote O_v formation at a lower potential, leading to superior OER activity in monolayer NiCo hydroxide.

Result and discussion

$Ni(acac)_2{\cdot}2H_2O$ is a typical layered molecular crystal, constructed by weak intermolecular hydrogen bonds (HBs) between H_2O and CH_3 (Fig. 1a). By removing the water of crystallization, all the methyl groups point outwards to form the surface of the $Ni(acac)_2$ monolayer molecular crystal. First-principles molecular dynamics confirmed that the monolayer structure is thermodynamically stable at finite temperature (Supplementary Fig. 1). Thus, a simple experiment was proposed in which bulk $Ni(acac)_2{\cdot}2H_2O$ was dispersed in an inert

[1]School of Chemistry, Beijing Advanced Innovation Center for Biomedical Engineering, Key Laboratory of Bio-Inspired Smart Interfacial Science and Technology, Beihang University, Beijing, China. [2]Beijing Computational Science Research Center, Beijing, China. [3]School of Physics, Beihang University, Beijing, China. [4]Jiangsu Key Laboratory for Carbon-based Functional Materials and Devices, Institute of Functional Nano and Soft Materials, Soochow University, Suzhou, China. [5]Center for High Pressure Science and Technology Advanced Research, Beijing, China. [6]Key Laboratory of Polar Materials and Devices, East China Normal University, Shanghai, China. [7]Department of Chemistry and Biochemistry, University of California, Los Angeles, Los Angeles, CA, USA. [8]These authors contributed equally: Jianxin Kang, Xiaoyi Qiu, Qi Hu. ✉e-mail: liminliu@buaa.edu.cn; guolin@buaa.edu.cn

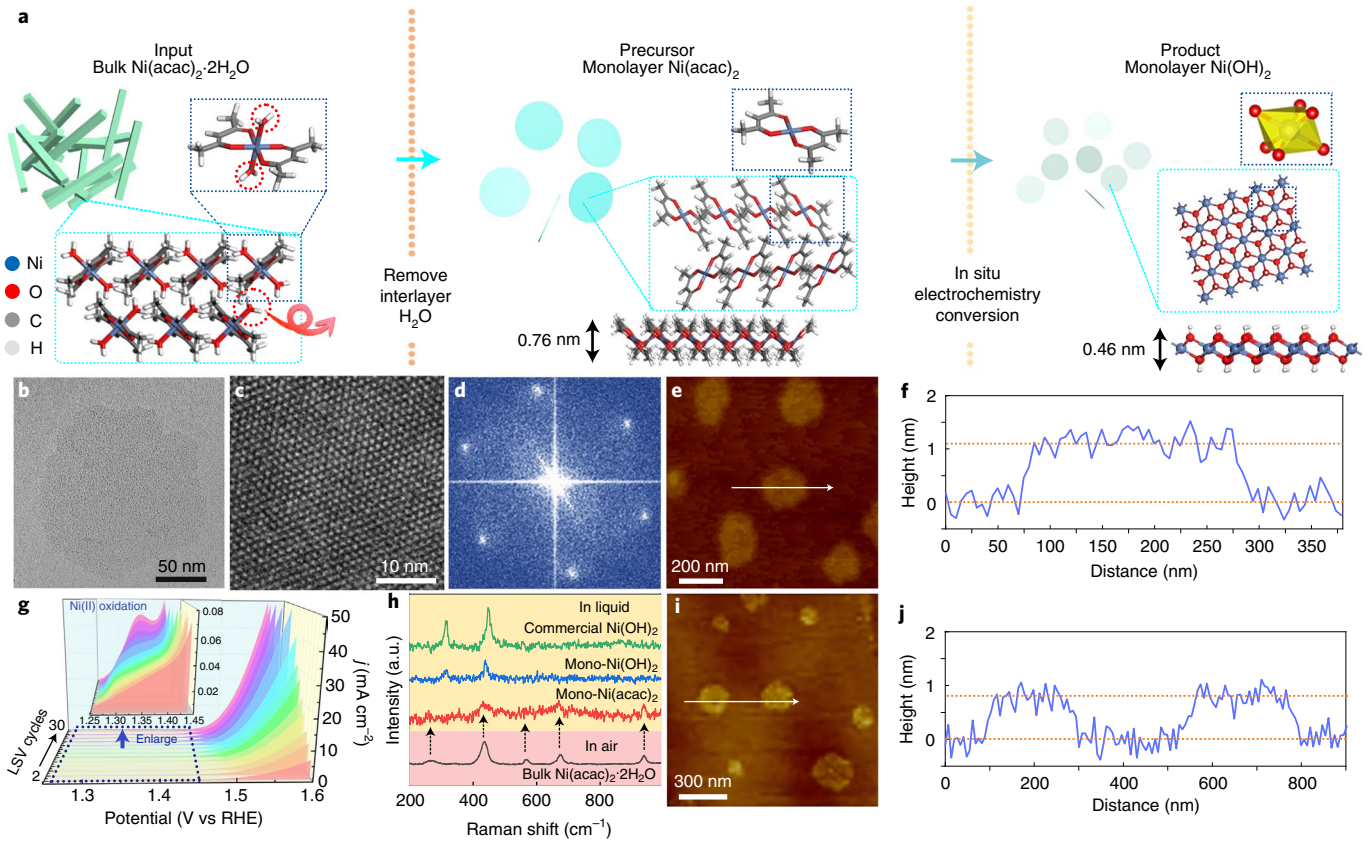

Fig. 1 | Schematic of the conversion from molecular crystal to monolayer hydroxide and structure characterization. a, Schematic illustration of the whole monolayer fabrication process, from the bulk organic molecular crystal of $Ni(acac)_2{\cdot}2H_2O$ to the monolayer molecular crystal and monolayer inorganic $Ni(OH)_2$. The corresponding atomic structures and theoretical thicknesses at each stage of the process are shown. **b**, TEM image of monolayer $Ni(acac)_2$. **c**,**d**, High-angle annular dark-field scanning transmission electron microscopy image (**c**) and the corresponding fast Fourier transform pattern (**d**) of monolayer $Ni(acac)_2$, showing the ordered crystal structure of the $Ni(acac)_2$ molecule. **e**,**f**, AFM image (**e**) and height profile (**f**) of monolayer $Ni(acac)_2$ nanosheets. **g**, Repeated LSV cycles of the exfoliated $Ni(acac)_2$ illustrate regular activation of the material. The inset shows a magnification of the LSV curves in the range 1.25–1.45 V, revealing the emergence of the oxidation peak. **h**, In situ Raman spectra demonstrating the structural changes along with the electrochemical decomposition that occur during the different stages of the fabrication process. Note, in all figures, monolayer and multilayer substrates are abbreviated to, for example, Mono-NiO_2 and Multi-NiO_2. **i**,**j**, AFM image (**i**) and height profile (**j**) of monolayer $Ni(OH)_2$ nanosheets.

organic solvent, such as anisole, diphenyl ether or dibutyl ether, then heated at the dehydration temperature (Supplementary Fig. 2) to remove intermolecular water (Supplementary Fig. 3). Thus, due to the destruction of the interlayer HBs, bulk $Ni(acac)_2{\cdot}2H_2O$ micro-rods (Supplementary Fig. 4) could be exfoliated to yield $Ni(acac)_2$ nanosheets (Fig. 1b). Infrared spectroscopy showed that all the organic groups were retained in the exfoliated nanosheets, with no apparent signal from hydroxy groups, indicating the removal of H_2O (Supplementary Figs. 5 and 6).

Low-voltage spherical aberration-corrected transmission electron microscopy (TEM) at a very low electron beam current clearly revealed the crystalline nature of monolayer $Ni(acac)_2$ (Fig. 1c,d). The experimental powder X-ray diffraction pattern of the as-prepared nanosheets was similar to the simulated pattern (Supplementary Fig. 7). Atomic force microscopy (AFM) was employed to confirm the monolayer nature of $Ni(acac)_2$ on a dismountable glassy carbon electrode (Supplementary Fig. 8), and height measurement revealed a monolayer thickness of 1.1 ± 0.4 nm (Fig. 1e,f), in agreement with the absolute theoretical monolayer thickness of 0.76 nm, excluding the van der Waals radius between the substrate and sample, determined by first-principles calculations. Because of the repulsive force between the organic groups of $Ni(acac)_2$, the monolayer $Ni(acac)_2$ nanosheets do not restack into multilayers in inert organic solvent.

Monolayer $Ni(acac)_2$ nanosheets dispersed in ethanol solution were then dropcast on a glassy carbon (GC) electrode. By precisely controlling the concentration of the monolayer $Ni(acac)_2$ nanosheets in the liquid dispersion, the monolayer $Ni(acac)_2$ nanosheets could be deposited on the electrode without restacking (Supplementary Fig. 9). The monolayer $Ni(acac)_2$ was then converted into monolayer $Ni(OH)_2$ by an in situ electrochemical conversion process through repeated cycles of linear sweep voltammetry (LSV) between 1.22 and 1.82 V versus the reversible hydrogen electrode (RHE) in 1 M KOH solution (Fig. 1g). With repeated LSV cycles, the Ni(II) redox peak[35] emerged after the 12th LSV cycle. In situ Raman study of the same sample position indicated that the initial organic $Ni(acac)_2$ gradually evolved into inorganic $Ni(OH)_2$ during this activation process (Fig. 1h and Supplementary Fig. 10), which was also verified by synchrotron X-ray absorption fine structure (XAFS) characterization and X-ray photoelectron spectroscopy (XPS; Supplementary Figs. 11 and 12). A similar electrochemical conversion process can be readily used to convert bulk $Ni(acac)_2$ into multilayer $Ni(OH)_2$ (Supplementary Fig. 13). TEM and electron energy loss spectroscopy (EELS) of the as-converted monolayer $Ni(OH)_2$ also confirmed the typical features of amorphous $Ni(OH)_2$ (Supplementary Fig. 14). Unambiguously characterizing the in situ conversion of a monolayer material with atomic thickness during in-liquid electrocatalysis is challenging. AFM indicated that the thickness is reduced by 0.3 nm

(from 1.1 ± 0.4 to 0.8 ± 0.4 nm) after the electrochemical conversion process (Fig. 1i,j), consistent with the thickness difference expected between monolayer $Ni(acac)_2$ (0.76 nm) and monolayer $Ni(OH)_2$ (0.46 nm). In situ AFM showed that monolayer $Ni(OH)_2$ is firmly anchored on the electrode without movement or restacking during and after the electrochemical conversion process, which represents an essential feature of our in situ conversion approach to achieving monolayer materials on electrodes (Supplementary Fig. 15). First-principles calculations indicated that monolayer $Ni(OH)_2$ nanosheets interact favourably with GC electrodes to ensure stable anchoring to the electrode surface without lifting off or restacking in solution (Supplementary Fig. 16).

To probe the evolution of the atomic and electronic structures in the electrochemical processes, we conducted in operando XAFS to investigate the valence state of Ni in mono- and multilayer $Ni(OH)_2$ at various electrochemical potentials; multilayer $Ni(OH)_2$ was synthesized as a control sample (Supplementary Fig. 17) and studied for comparison. The Ni K-edge X-ray absorption spectroscopy (XAS) main peak (white line peak) at ~8,344 eV can be attributed to the electronic transition from 1*s* to the unoccupied 4*p* orbital. Because a higher oxidation state typically leads to a higher binding energy, the Ni K-edge XAS main peak related to the Ni 1*s* binding energy normally shifts to a higher absorption energy with a higher oxidation state, as widely reported in the literature[36–38]. With increasing anodic potential from 1.30 to 1.50 V, the Ni K-edge of monolayer $Ni(OH)_2$ progressively shifted to a higher energy (Fig. 2a). In contrast, the Ni K-edge of multilayer $Ni(OH)_2$ did not show any significant change until reaching a high potential of >1.55 V (Fig. 2b). By using $Ni(OH)_2$ and $LaNiO_3$ as reference positions of Ni(II) and Ni(III), respectively (Supplementary Figs. 18 and 19)[36], we further quantified the change in valence state as a function of anodic potential. Notably, monolayer $Ni(OH)_2$ crossed to the Ni(III) state at a potential as low as 1.35 V (Fig. 2c), starting to generate the high-valence state Ni(IV), whereas multilayer $Ni(OH)_2$ showed a constant low-valence state below Ni(III) at potentials of <1.50 V. It is noted that its average valence state did not reach Ni(III) until a potential of >1.55 V, and no Ni(IV) was observed within our potential sweep range (Fig. 2c). Thus, the monolayer material reached oxidation states Ni(III) and Ni(IV) at lower potentials, which is beneficial for the OER process[24,39,40].

The increased valence state of Ni in $Ni(OH)_2$ is fundamentally related to the dehydrogenation process. From Ni(II) to Ni(III) and Ni(IV), one or two hydrogen atoms need to be removed per formula unit $Ni(OH)_2$. In monolayer $Ni(OH)_2$, the hydrogen atoms are fully exposed to solution and can detach and move directly into solution upon reaching a proper electrochemical potential. In contrast, in multilayer $Ni(OH)_2$, the hydrogen atoms need to diffuse from the interior region to the surface or edge before participating in the dehydrogenation process (Fig. 2d). The calculated hydrogen diffusion barrier in $Ni(OH)_2$ is about 0.21 eV, and the hydrogen diffusion barrier in NiOOH can reach up to 1.16 eV. Such diffusion barriers represent an additional energy barrier to the dehydrogenation process in multilayers. Notably, our experimental studies show that an extra potential of ~0.2 V is required to dehydrogenate one hydrogen atom from multilayer $Ni(OH)_2$ (compared with in monolayers) to reach an average valence state of Ni(III); and few hydrogen can be detached from the multilayer NiOOH to access Ni(IV) due to the much higher hydrogen diffusion barrier. This is largely consistent with our theoretical predictions.

Without the sluggish hydrogen diffusion in monolayer $Ni(OH)_2$, dehydrogenation can readily occur at a considerably lower potential to access high-valence Ni(III) and Ni(IV), which is critical for the water oxidation process. Indeed, monolayer $Ni(OH)_2$ shows a much lower overpotential ($\eta_0 = 276$ mV at 10 mA cm^{-2}) than multilayer $Ni(OH)_2$ (956 mV) or unexfoliated $Ni(acac)_2{\cdot}2H_2O$ (674 mV), and even better than those with a 1,000 times higher loading on carbon paper (573 and 297 mV; Fig. 2e). As shown below, the overpotential of the monolayer can be further decreased by heteroatom doping. Further analysis showed a mass activity of ~8×10^4 A g^{-1} and a turnover frequency (TOF) at $\eta = 300$ mV of up to ~20 s^{-1}, both of which are considerably higher than those values reported previously for Ni-based OER catalysts[24,37,41–44].

The oxygen evolution process involves the escape of an oxygen atom and the formation of O_v, which produces active sites and in turn greatly affects the OER performance[21–24,38]. Therefore, we conducted further first-principles calculations to explore whether the monolayer geometry could also facilitate the escape of oxygen atoms and enhance the formation of O_v as compared with multilayers. We calculated the formation energies of O_v (E_{Ov})[45] and the corresponding electronic structures (Fig. 3). The generation of O_v under an applied voltage led to an upshift of the valence band of NiOOH (Supplementary Fig. 20). Our calculations revealed that the E_{Ov} values in monolayer $Ni(OH)_2$ and NiOOH are, respectively, about 0.33 and 0.11 eV lower than those in their multilayer counterparts due to the lack of HBs in the monolayers. In contrast, mono- and multilayer NiO_2 have comparable E_{Ov} values. Meanwhile, the calculated E_{Ov} values for each step of the OER reaction and the energy barriers for O_v formation through O_2 detachment also have low values (Supplementary Figs. 21 and 22). Thus, these calculations clearly suggest that O_v would form more readily in monolayer $Ni(OH)_2$ and NiOOH than in multilayer $Ni(OH)_2$ and NiOOH, contributing to the higher OER activity.

Previous experimental studies have shown that heteroatom doping with group VIII elements to form bimetallic hydroxides could considerably modify or boost OER performance[37,41,42]. With the metal ion exposed at the edge of the basal plane, edge minority facets have been widely explored by first-principles calculations[46,47], with a theoretical overpotential of 0.30 V predicted with heterometal doping, which is lower than the values typically expected for the basal facet. Following the successful preparation of monolayers with dominant basal planes, we considered Co-doped $Ni(OH)_2$ to explore the activity of the basal facet in the monolayer. Our calculations show that Co doping increases E_{Ov} in $Ni(OH)_2$, but considerably decreases E_{Ov} in NiOOH by 0.18 eV and E_{Ov} in NiO_2 by 0.20 eV (Fig. 3i). Thus, Co doping could greatly enhance O_v formation in monolayer NiOOH and NiO_2. Because O_v formation in NiOOH and NiO_2 is critical for the OER process, it is expected that Co doping could further boost OER catalytic activity.

To this end, we explored monolayer bimetallic NiCo hydroxide produced by a similar process with $Co(acac)_2{\cdot}2H_2O$ and $Ni(acac)_2{\cdot}2H_2O$ as precursors. TEM, energy dispersion spectroscopy (EDS) and AFM (Supplementary Figs. 23 and 24) revealed a typical monolayer molecular crystal structure and the uniform distribution of the two elements in a Co/Ni ratio of about 1:1. XAFS and XPS also suggested the formation of NiCo hydroxide (Supplementary Figs. 25 and 26). The in operando XAFS spectra revealed an intriguing oscillation of the energy of the absorption edge of Ni in the monolayer NiCo hydroxide with increasing potential (Supplementary Fig. 27a). Similarly, the absorption edge of Co atoms in the Co-doped monolayer also showed abnormal oscillations (Supplementary Fig. 27b). From the shift of the Ni and Co K-edge positions observed in in situ studies, we determined the evolution of the Ni and Co valence states in monolayer NiCo hydroxide, both of which exhibited an unusual oscillation with increasing potential. Specifically, the valence state of Ni in NiCo hydroxide increased with increasing potential from 0 to 1.35 V, then exhibited a notable drop in the potential range of 1.35 to 1.40 V (Fig. 3j). The valence state of Co in NiCo hydroxide also showed a similar increase from 0 to 1.30 V, followed by a decrease from 1.30 to 1.35 V, ~0.05 V earlier than in the case of Ni (Fig. 3k). The valence state of Ni in pure monolayer $Ni(OH)_2$ exhibited a similar feature to that of NiCo hydroxide before 1.35 V, but did not show the apparent decrease in valence state beyond 1.35 V, with only a

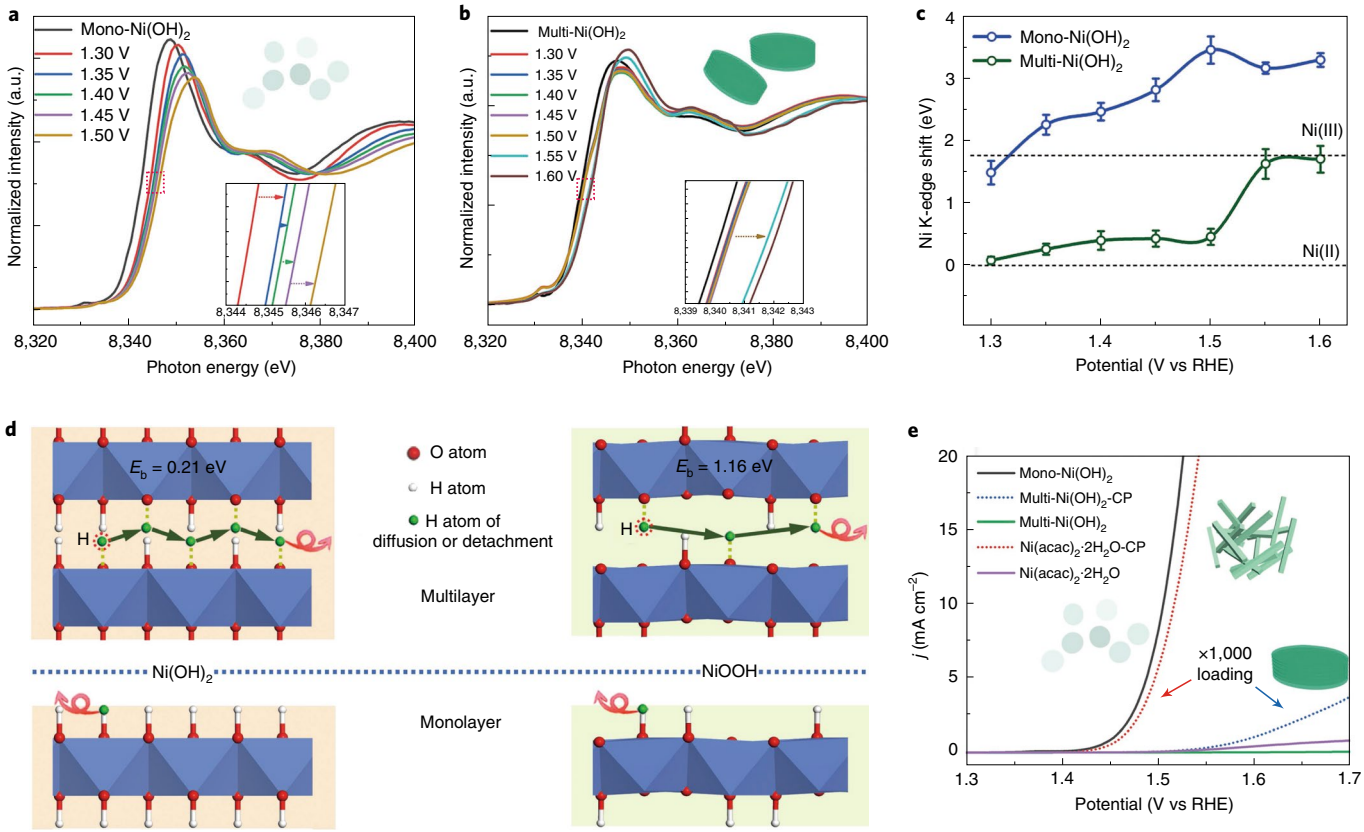

Fig. 2 | Relationship between the valence states of Ni and the dehydrogenation of mono- and multilayer $Ni(OH)_2$. a,**b**, In operando XAFS spectra of monolayer $Ni(OH)_2$ (**a**) and multilayer $Ni(OH)_2$ (**b**) showing the Ni K-edge, recorded during potentiostatic OER experiments in 1 M KOH at various potentials. The insets show a magnification of the spectra in the highlighted squares. The arrows show the shift of the edge position with increasing potential. **c**, Shift in the Ni K-edge position of monolayer and multilayer $Ni(OH)_2$ from the valence state Ni(II). $Ni(OH)_2$ and $LaNiO_3$ were employed as references for Ni(II) and Ni(III), respectively. The error bars represent the standard deviation of three sets of data. **d**, The calculated hydrogen diffusion process from the interior to the edge in multilayer $Ni(OH)_2$ and NiOOH (top). The hydrogen diffusion barriers (E_b) calculated for multilayer $Ni(OH)_2$ (0.21 eV) and NiOOH (1.16 eV) are shown. The monolayer is shown for comparison (bottom). In this case, hydrogen diffusion is not required before detachment. The blue frames represent the crystal field of the Ni atoms. **e**, LSV curves of monolayer $Ni(OH)_2$ and other catalysts loaded onto GC electrodes or carbon paper (CP).

reduced increasing slope in the range 1.35–1.50 V (Fig. 3j). For multilayer $Ni(OH)_2$, the increase in the valence state did not occur until a higher potential, beyond 1.50 V (Fig. 3j). As for Co, changes in the valence state in pure multilayer CoOOH could barely be observed in the applied potential range (Fig. 3k).

Overall, as a general trend, the valence state of Ni in the Co-doped material increased quickly from Ni(II) to Ni(III), followed by a slow increase or even a decrease with further increasing potential. After this, the valence state resumed a rapid increase from Ni(III) to Ni(IV). The previously discussed dehydrogenation would lead to a progressive increase in the valence state; the decrease in the valence state is thus attributed to deoxygenation and the in situ formation of O_v. Electron paramagnetic resonance (EPR) spectroscopy is very sensitive to O_v generation and concentration[11,19]. The EPR spectrum of the NiCo hydroxide after the OER exhibits an obviously larger peak at $g = 2.002$ than the spectrum before the OER, which indicates O_v generation during the OER (Supplementary Fig. 28). In addition, the formation of O_v was also confirmed by the O K-edge XAS data (Supplementary Fig. 29). When oxygen atoms escape, the resulting O_v could produce extra electrons in the surrounding metal atoms, which lowers the valence state of the metal atoms.

The role of Co doping in promoting O_v formation can be understood in terms of the electronic structure. For Ni(III) in pure NiOOH, the electronic configuration is $t_{2g}^6e_g^1$, and the d_{z^2} orbital is occupied in a distorted crystal field due to the Jahn–Teller effect (Fig. 3a,b and Supplementary Fig. 30). The doped Co(III) atoms are in a distorted octahedral crystal field dictated by the NiOOH matrix, induced by the asymmetric $t_{2g}^5e_g^1$ filling of Co(III). Considering that the energy level of the unoccupied $d_{x^2-y^2}$ orbital of Co(III) is lower than that of Ni(III) by about 0.15 eV (Supplementary Fig. 31), the excess electron prefers to occupy the lowest unoccupied orbital of Co(III), resulting in the conversion of Co(III) into Co(II). The same conclusion can be drawn for Co(IV) (Fig. 3b–h). Thus, the doped Co(III)/Co(IV) in the distorted crystal field is easier to reduce to a lower valence state than Ni(III)/Ni(IV), which promotes O_v formation around the Co atom. Meanwhile, considering that Co(III) and Co(IV) are prone to capture excess electrons, the valence state of Co should first decrease as O_v is generated, followed by the valence state of Ni, consistent with the XAFS studies described above.

To explore the influence of O_v in the OER process, we investigated the free energies (ΔG) of the four-electron OER process for pure and Co-doped systems without and with O_v (Fig. 4a–c). The release of one O or OH from NiOOH creates three exposed metal ions, where further adsorption and reaction could occur. We calculated the overpotentials for all possible active sites, as shown in the volcano plot in Fig. 4b. In the case of perfect monolayer NiOOH without O_v, the calculated overpotential for the OER is 0.68 V; the introduction of O_v substantially reduces the overpotential to 0.38 V.

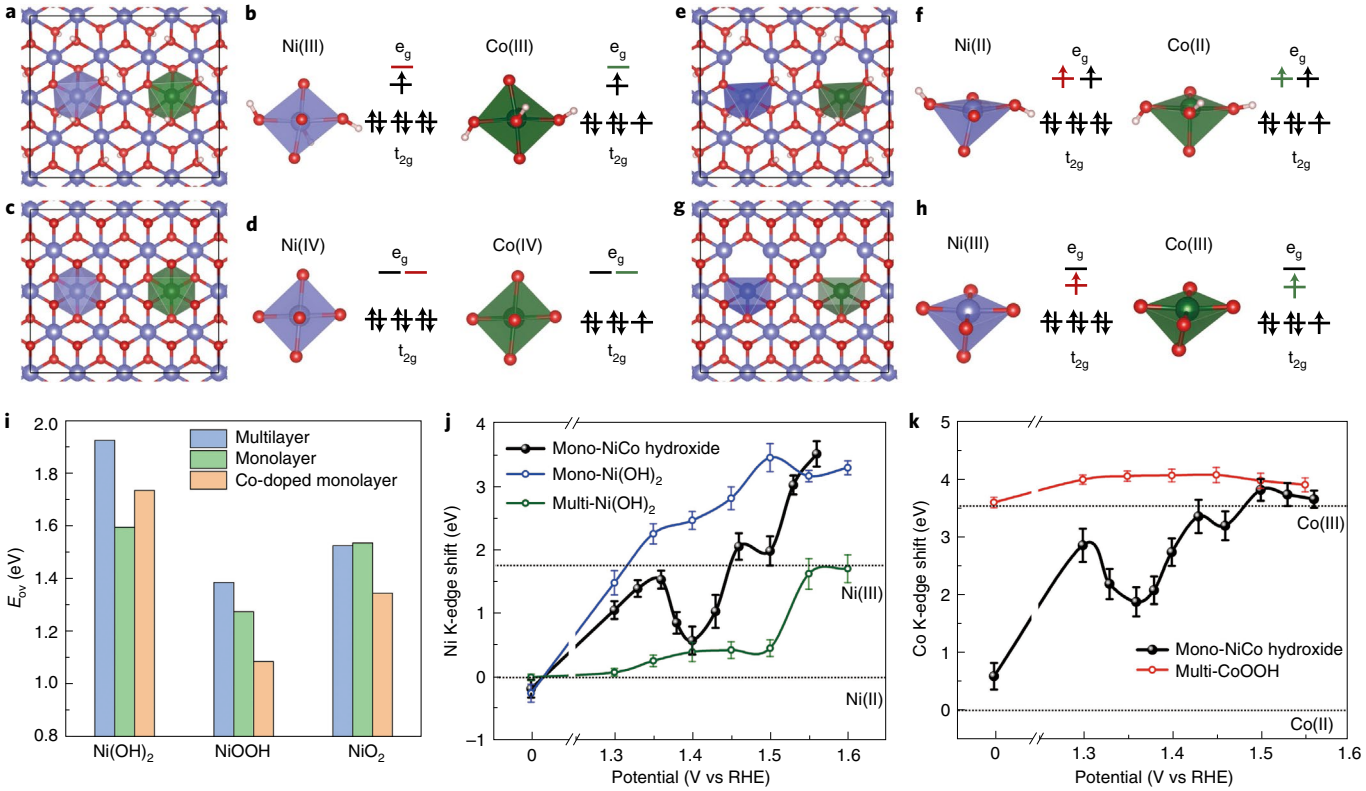

Fig. 3 | Production and detection of in situ generated oxygen vacancies by the release of oxygen atoms. a–h, Atomic structures (**a**,**c**,**e**,**g**) and the corresponding electronic configurations (**b**,**d**,**f**,**h**) of the metal cations in Co-doped systems: NiOOH (**a**,**b**), NiO_2 (**c**,**d**), NiOOH with O_v (**e**,**f**) and NiO_2 with O_v (**g**,**h**). The H, O, Ni and Co atoms are represented by white, red, blue and green balls, respectively. **i**, Calculated E_{Ov} values for multilayer $Ni(OH)_2$ and pure or Co-doped monolayer $Ni(OH)_2$ in different valence states. **j**, In operando Ni K-edge shifts observed for monolayer NiCo hydroxide, monolayer $Ni(OH)_2$ and multilayer $Ni(OH)_2$ compared with the Ni(II) K-edge, recorded during potentiostatic OER experiments in 1 M KOH at various potentials. **k**, In operando Co K-edge shifts observed for monolayer NiCo hydroxide and multilayer CoOOH compared with the Co(II) K-edge, recorded during potentiostatic OER experiments in 1 M KOH at various potentials. $Co(OH)_2$ and CoOOH were employed as references for Co(II) and Co(III), respectively. The error bars in **j** and **k** represent the standard deviation of three separate sets of data.

On the other hand, the formation of O_v in Co-doped NiOOH further decreases the overpotential to 0.35 V (Fig. 4b), indicating that O_v play a significant role in the OER process. A similar trend was found for NiO_2 (Supplementary Fig. 32). Thus, the formation of O_v is vital for producing active sites and decreasing the overpotential and boosting OER activity. Overall, the lowest overpotential that can be expected for Co-doped NiOOH with O_v is 0.35 V, approaching the theoretical peak of the OER volcano[17,48] (Fig. 4b). The optimal reaction pathway for Co-doped NiOOH with O_v is shown in Fig. 4c.

As discussed above, E_{Ov} is lower by only 0.11 eV in monolayer NiOOH compared with in the multilayer; thus, the monolayer should slightly promote O_v formation. By contrast, Co doping effectively enhances O_v formation by greatly reducing E_{Ov} (Fig. 3i). Considering that O_v correlate with activity, monolayer $Ni(OH)_2$ decreases the overpotential only a little, as observed in the above experiment, whereas the Co-doped system reduces the overpotential further. The onset potential of NiCo hydroxide was experimentally determined to be 1.38 V (Fig. 4d), which is just beyond the potential of the minimum valence state of Co detected by in situ XAFS (~1.35 V; Fig. 3k). Similarly, the onset potential of pure $Ni(OH)_2$ was determined to be 1.42 V, also just slightly above the valence state valley (~1.40 V; Fig. 3j). The observed decrease, or slow increase, in the valence state originates from O_v formation, as discussed above. Thus, the O_v generated before the OER process, associated with valence state oscillation, is believed to dynamically create the active sites for triggering the oxygen evolution.

With the easier dehydrogenation and reduced formation energy of O_v, monolayer NiCo hydroxide on a GC electrode required an overpotential of only 208 mV to achieve a current density of 10 mA cm^{-2}, with a high Faradaic efficiency of ~99% (Fig. 4d and Supplementary Figs. 33–35). To understand the origin of the high activity, the electrochemical active surface area (ECSA) and specific activity of the catalysts were also evaluated from the double-layer capacitance of the system (Fig. 4e, Supplementary Fig. 36 and Supplementary Table 1)[49]. The ECSA of monolayer $Ni(OH)_2$ was determined to be more than three times higher than that of multilayer $Ni(OH)_2$. With the same loading, monolayer NiCo hydroxide exhibits an ECSA more than two times higher than that of monolayer $Ni(OH)_2$. This indicates that both the monolayer and Co doping can effectively increase the number of active sites. Furthermore, very high specific activities (j_s) of 26.3 and 37.7 mA cm^{-2} at $\eta = 350$ mV were calculated for both monolayer NiCo hydroxide and pure $Ni(OH)_2$, respectively, which are several orders of magnitude higher than those of multilayer $Ni(OH)_2$ and most reported OER catalysts[49].

We recognized that monolayer loading on GC electrodes leads to a limited number of active sites. To this end, we further loaded our optimized monolayer catalysts onto highly porous Cu foam to reduce resistance (Supplementary Fig. 37), and further reduced the overpotential to 183 mV, which is among the lowest overpotentials ever reported. With comparable overpotentials to the best reported OER catalysts at much lower mass loading of the active LDH catalysts (~1 μg cm^{-2} in our study compared with 0.2–10 mg cm^{-2}

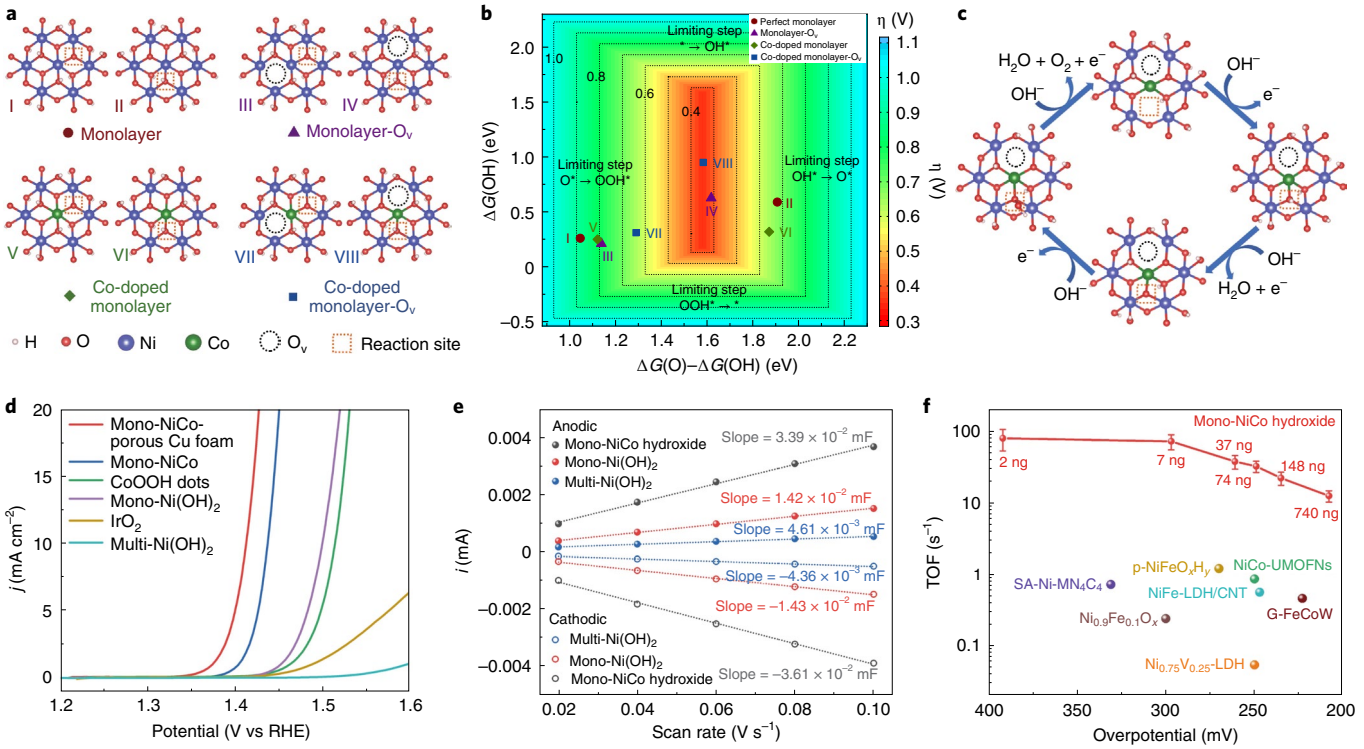

Fig. 4 | Promotion of OER activity induced by in situ generated Ov. a, The possible reactive sites for the different monolayer NiOOH systems. Structures I–IV represent monolayer NiOOH systems, and structures V–VIII show Co-doped monolayer NiOOH systems. **b**, Theoretical overpotential volcano plot for NiOOH with O* and OH* binding energies (ΔG_O and ΔG_{OH}) as descriptors, using the scaling relationship between OH* and OOH* ($\Delta G_{OOH} = \Delta G_O + 3.16$ eV). All calculated overpotentials for the different sites of the pure, O_v and Co-doped monolayer systems shown in **a** are contoured. Here, O*, OH* and OOH* stand for the corresponding adsorption states. **c**, Optimal reaction pathway for Co-doped NiOOH with O_v. **d**, LSV curves of different hydroxide catalysts, compared with that of IrO_2. **e**, The anodic and cathodic charging currents measured by cyclic voltammetry at 1.06 V versus RHE, plotted as a function of scan rate. The slopes are equal to the double-layer capacitance. **f**, Plot of the catalytic activity of monolayer NiCo hydroxide with different loading amounts, from ~2 ng (left) to ~740 ng (right), compared with those of recently reported OER catalysts (refs. [17,24,37,41–44]). Here, SA, p, UMOFNs, CNT and G stand for single atom, particle, ultrathin metal organic framework nanosheets, carbon nanotube and gelled, respectively. The *x* axis shows the overpotential required to achieve 10 mA cm^{-2}, and the *y* axis is the TOF value at $\eta = 300$ mV. The error bars represent the standard deviation of three separate sets of data.

in previous studies), we expected a much higher intrinsic activity for our monolayer NiCo hydroxide and thus further evaluated the TOF of the monolayer NiCo hydroxide. Significantly, monolayer NiCo hydroxide catalysts, with different loadings, exhibited remarkable TOFs of ~10–70 s^{-1} (Fig. 4f), about two orders of magnitude higher than most LDH catalysts reported to date, including single atom catalysts[17,24,37,41–44]. We should note that although monolayer and few-layer LDHs have been reported before[37,42,44,50], restacking and aggregation of monolayers usually occur during loading on the electrode, resulting in few-layer or even multilayer LDHs with seriously compromised electrocatalytic performance. In contrast, in situ electrochemical conversion ensures the direct formation of monolayer NiCo hydroxides on electrodes, offering a robust system for fundamental investigation of monolayer materials, and provides ultrahigh TOFs that are orders of magnitude higher than previous reports. Long-time chronopotentiometry was carried out at $J = 10$ mA cm^{-2} for 180 h to evaluate the stability of the electrodes, and the results show that the working potential remained almost constant for the entire testing period, demonstrating excellent electrochemical durability (Supplementary Fig. 38).

Conclusion

We have reported here an in situ conversion process for directly preparing monolayer LDHs on electrodes, defining a robust material platform for exploring the fundamental reaction mechanism in monolayer LDH-based electrocatalysts. Our systematic experimental and theoretical studies revealed Ni and Co valence state oscillation in monolayer NiCo hydroxides, which is attributed to sequential dehydrogenation and deoxygenation processes and fundamentally contributes to the dynamic generation of OER active sites. Furthermore, our studies have revealed that heteroatom doping by Co allows further tuning of the *d* electronic structure through the Jahn–Teller effect, reducing the dehydrogenation/deoxygenation potential and activating oxygen atoms at lower potential, further reducing the overpotential of the OER. Such understanding offers important fundamental insights for the design of highly active LDH-based electrocatalysts and could have far-reaching impacts on this increasingly important topic.

Methods

Synthesis of monolayer Ni(acac)$_2$. In a typical synthesis of monolayer Ni(acac)$_2$, 6 mg Ni(acac)$_2$·2H$_2$O was first introduced into a flask containing 30 ml predried anisole (other inert organic solvents such as diphenyl ether and dibutyl ether could also be used) and stirred for 1 h at 30 °C to form a green solution. Afterwards, the mixture was rapidly heated to 90 °C and held at this temperature for ~15 min. After cooling to room temperature, the solution was centrifuged at 12,000 r.p.m. and washed with the same inert organic solvent three times. In particular, there was almost no solid visible after each centrifugation, so the bottom 10% liquid in the centrifuge tube was gathered for the next washing. Finally, a colourless solution was obtained for further analysis.

Synthesis of monolayer NiCo-acetylacetonate. In a typical synthesis of monolayer NiCo-acetylacetonate, 4 mg Ni(acac)$_2$·2H$_2$O and 4 mg Co(acac)$_2$·2H$_2$O were introduced into a flask containing 30 ml predried anisole (other inert organic

solvents such as diphenyl ether and butyl ether could also be used) and stirred for 1 h at 30 °C to give a pink solution. Afterwards, the mixture was rapidly heated to 90 °C and then held at this temperature for ~12 min. After cooling to room temperature, the solution was centrifuged at 12,000 r.p.m. and washed with the same inert organic solvent three times. In particular, there was almost no solid visible after each centrifugation, so the bottom 10% liquid in the centrifuge tube was gathered for the next washing. Finally, a colourless solution was obtained for further analysis.

Monolayer loading of hydroxide. After quantification by inductively coupled plasma atomic emission spectrometry (ICP-AES), a certain amount of monolayer $Ni(acac)_2$ or NiCo-acetylacetonate solution was dispersed in ethanol and dropped onto a hydrophilic GC electrode (diameter 5 mm). After volatilization under heating, the dried GC electrode was employed as a working electrode. Combining with a Pt wire and Ag/AgCl electrode as the counter and reference electrode, respectively, electrochemical in situ decomposition was carried out in a standard three-electrode system in 1 M KOH electrolyte (controlled by a Pine Instruments electrochemistry workstation). LSV was carried out at 20 mV s^{-1} in the voltage range 0–0.6 V; the whole decomposition process required ~12 cycles. The emergence of the typical Ni(II)/Ni(III) redox peak at ~0.30–0.40 V indicated that conversion was accomplished.

XAFS analysis. XAFS spectra at the Ni and Co K-edges were collected at the 1W1B beamline station of the Beijing synchrotron radiation facility (BSRF). The storage ring of the BSRF was operated at 2.5 GeV with a maximum current of 300 mA. Fixed-exit Si (111) double crystals were used as monochromator. The XAFS spectra were collected in fluorescence mode with ionization chambers filled with Ar/N_2 at room temperature. The energies were calibrated using Ni and Co foils.

In situ XAFS spectra of the monolayer hydroxides and multilayer $Ni(OH)_2$ were collected using an in operando electrochemical cell (EC-FXAS-VI, Beijing Scistar Technology). The in operando electrochemical cell was made of polyether ether ketone (PEEK), a chemically inert material with good mechanical properties and electrical insulation. In this operando cell, a Pt wire and Ag/AgCl electrode were used as the counter and reference electrode, respectively. Thin carbon paper loaded with $Ni(OH)_2$ with a quadrate window (1 cm × 1 cm) covered with Kapton film was employed as the working electrode. During the measurements, a series of potentials were applied to the working electrode in 1 M KOH solution. In operando XAFS measurements were collected at each potential over ~12 min.

Ni and Co K-edge theoretical X-ray absorption near-edge structure spectra were simulated within the framework of multiple-scattering theory using the FEFF9 code within the muffin-tin approximation. Extended X-ray absorption fine structure data processing and analysis were completed using the Athena and Artemis software from the IFEFFIT package.

XAS spectra at the O K-edge were collected at the National Synchrotron Radiation Laboratory (Beamlines MCD-A and MCD-B, Soochow Beamline for Energy Materials).

Electrochemical measurements. GC electrodes loaded with the decomposed monolayer hydroxide were employed as working electrodes for the electrochemical measurements. The loading amount was calculated from the concentration of the solution, which was confirmed by ICP-AES. In a typical experiment, the loading was 74 ng catalyst. Combining with a Pt wire and Ag/AgCl electrode as the counter and reference electrode, respectively, electrochemical studies were carried out in a standard three-electrode system (controlled by a Pine Instruments electrochemistry workstation). A 1 M KOH aqueous solution was used as the electrolyte in all the electrochemical measurements. In this report, the potentials are given versus RHE using the RHE calibration: $E(\mathrm{RHE}) = E(\mathrm{Ag/AgCl}) + 0.197 + 0.0591 \times \mathrm{pH}$, where pH = 14 in the 1 M KOH solution. The working electrode was rotated at 1,600 r.p.m. to disperse the generated oxygen bubbles.

Chronopotentiometric measurements were recorded at a current density of 10 mA cm^{-2}.

Electrochemical impedance spectroscopy was performed at 0.5 V versus Ag/AgCl on the GC electrode. The amplitude of the sinusoidal wave was 10 mV, and the frequency scan range was 100 kHz to 0.01 Hz. The measured impedance data were fitted using a series R(QR)(QR) equivalent circuit. All polarization curves were corrected with 95% *iR* compensation, where $R = 6\,\Omega$ in 1 M KOH.

TOFs were calculated from the following equation:

$$\mathrm{TOF} = J \times A/(4 \times F \times n) \quad (1)$$

where J is the current density at an overpotential of 300 mV, A is the area of the GC electrode, F is the Faraday constant and n is the number of moles of catalyst deposited on the GC electrode, which was calculated from the concentration of the solution. In this work, all the catalysts were assumed to be active.

The Faradaic efficiency was evaluated by the rotating ring disk electrode method and calculated from the following equation:

$$\text{Faradaic efficiency} = I_{\mathrm{ring}}/(C_{\mathrm{e}} \times I_{\mathrm{disk}}) \quad (2)$$

where I_{disk} is the input current given on the GC electrode, I_{ring} is the collected current on the Pt wire electrode at a constant potential of 0.4 V versus RHE and C_{e} is the oxygen collection coefficient (~0.2) for this type of electrode configuration.

The ECSA was determined by measuring the capacitive current associated with double-layer charging by cyclic voltammetry at different scan rates in a non-Faradaic potential range. In a typical experiment, the potential window of the cyclic voltammograms was 0–0.1 V versus Ag/AgCl (1 M KOH). The scan rates were 20, 40, 60, 80 and 100 mV s^{-1}. The ECSA was determined by plotting the anodic and cathodic currents measured at 0.05 V versus Ag/AgCl (1 M KOH) against the scan rate. The average slope represents C_{DL}.

The specific activity (j_s) was calculated by dividing the current density per geometric area (j_g) at $\eta = 350$ mV by the determined roughness factor, which is the quotient of the ECSA and geometric area. In a typical experiment, the electrode was a 5-mm GC electrode with a geometric area of 0.196 cm^2.

In situ Raman measurements. In situ Raman spectra were collected using an in operando electrochemical cell (EC-Raman-VI, Beijing Scistar Technology). The in situ electrochemical cell was made of PEEK, a chemically inert material with good mechanical properties and electrical insulation. In this in situ cell, a Pt wire and Ag/AgCl electrode were used as counter and reference electrode, respectively. A GC electrode (thickness of 500 nm) with loaded catalyst and a round window (diameter 2 cm) covered by a quartz plate was employed as the working electrode. A 1 M KOH aqueous solution was used as the electrolyte, which was driven by a peristaltic pump to flow around the catalyst on the GC electrode to remove the generated bubbles. During measurement, a series of potentials were applied to the working electrode.

Spherical aberration-corrected TEM measurements. Spherical aberration-corrected TEM samples were prepared by delivering monolayer molecular crystal nanosheets onto a copper grid covered with carbon nanotubes. TEM and scanning transmission electron microscope (STEM) studies were carried out using a spherical aberration-corrected JEM-ARM300F microscope (JEOL) operating at 80 kV. A convergence angle of 30 mrad and an inner detector angle larger than 70 mrad were used for high-angle annular dark-field STEM (HAADF-STEM) imaging. To minimize the structural damage caused by electron beam irradiation, fast HAADF-STEM imaging was performed using a short dwell time of 6 µs and a small probe current of 5 pA.

First-principles calculations. Calculations were performed using first-principles density functional theory (DFT), as implemented in the Vienna Ab initio Simulation Package[51]. The atomic coordinates of the optimized computational models are provided in the Supplementary Data files. PBE+U was used for the calculations and a simple Hubbard U correction term was used to improve the interactions between strongly localized electrons. The corresponding U values were 6.7 eV and 5.5 eV for Co and Ni, respectively[52,53]. A plane-wave cut-off of 500 eV was applied to expand the electron wave functions. The vacuum layers were set to 10 Å to avoid periodic interactions. The reciprocal space was sampled using a 3 × 3 × 3 mesh grid by using the Monkhorst–Pack k-point scheme. The structures were relaxed until the total energy variation was less than 10^{-6} eV and all forces on each atom were less than 0.01 eV $Å^{-1}$. The van der Waals density functional[54] approach was used to describe the van der Waals interactions.

The OER can occur through a four-electron reaction in alkaline media in the following elementary steps[45]:

$$\mathrm{OH^-} + {}^* \rightarrow {}^*\mathrm{OH} + \mathrm{e^-} \quad (3)$$

$${}^*\mathrm{OH} + \mathrm{OH^-} \rightarrow {}^*\mathrm{O} + \mathrm{H_2O} + \mathrm{e^-} \quad (4)$$

$${}^*\mathrm{O} + \mathrm{OH^-} \rightarrow {}^*\mathrm{OOH} + \mathrm{e^-} \quad (5)$$

$${}^*\mathrm{OOH} + \mathrm{OH^-} \rightarrow \mathrm{O_2} + \mathrm{H_2O} + \mathrm{e^-} \quad (6)$$

For each electron-transfer step, the free-energy change (ΔG) can be expressed as follows:

$$\Delta G = \Delta E + \Delta \mathrm{ZPE} - T\Delta S \quad (7)$$

where ΔE, ΔZPE, $T\Delta S$ and U represent the energy change, zero-point energy correction, entropic energy and applied potential versus RHE, respectively.

The oxygen vacancy formation energy (E_{Ov}) was calculated as follows:

$$E_{\mathrm{Ov}} = E_{\mathrm{slab\_Ov}} - E_{\mathrm{perfect}} + 1/2E_{\mathrm{O_2}} \quad (8)$$

where $E_{\mathrm{slab\_Ov}}$ and E_{perfect} are the total DFT energies of the defect and perfect NiCo hydroxide systems, respectively, and $E_{\mathrm{O_2}}$ is the total energy of O_2.

Data availability

The data supporting the findings of this study are available in the paper and its Supplementary Information. Additional data are available from the corresponding authors upon reasonable request.

Received: 23 July 2020; Accepted: 26 October 2021;
Published online: 6 December 2021

References

1. Mannix, A. J., Kiraly, B., Hersam, M. C. & Guisinger, N. P. Synthesis and chemistry of elemental 2D materials. *Nat. Rev. Chem.* **1**, 0014 (2017).
2. Coleman, J. N. et al. Two-dimensional nanosheets produced by liquid exfoliation of layered materials. *Science* **331**, 568–571 (2011).
3. Yu, Y. et al. High-temperature superconductivity in monolayer $Bi_2Sr_2CaCu_2O_{8+\delta}$. *Nature* **575**, 156–163 (2019).
4. Ji, D. et al. Freestanding crystalline oxide perovskites down to the monolayer limit. *Nature* **570**, 87–90 (2019).
5. Gao, S. et al. Partially oxidized atomic cobalt layers for carbon dioxide electroreduction to liquid fuel. *Nature* **529**, 68–71 (2016).
6. Duan, H. H. et al. Ultrathin rhodium nanosheets. *Nat. Commun.* **5**, 3093 (2014).
7. Li, J. et al. General synthesis of two-dimensional van der Waals heterostructure arrays. *Nature* **579**, 368–374 (2020).
8. Manzeli, S., Ovchinnikov, D., Pasquier, D., Yazyev, O. V. & Kis, A. 2D transition metal dichalcogenides. *Nat. Rev. Mater.* **2**, 17033 (2017).
9. Zhou, J. et al. A library of atomically thin metal chalcogenides. *Nature* **556**, 355–359 (2018).
10. Tan, C. et al. Recent advances in ultrathin two-dimensional nanomaterials. *Chem. Rev.* **117**, 6225–6331 (2017).
11. Zhao, Y. et al. Layered-double-hydroxide nanosheets as efficient visible-light-driven photocatalysts for dinitrogen fixation. *Adv. Mater.* **29**, 1703828 (2017).
12. Luo, J. et al. Water photolysis at 12.3% efficiency via perovskite photovoltaics and earth-abundant catalysts. *Science* **345**, 1593–1596 (2014).
13. Roger, I., Shipman, M. A. & Symes, M. D. Earth-abundant catalysts for electrochemical and photoelectrochemical water splitting. *Nat. Rev. Chem.* **1**, 0003 (2017).
14. Seh, Z. W. et al. Combining theory and experiment in electrocatalysis: insights into materials design. *Science* **355**, eaad4998 (2017).
15. Gao, J. et al. Breaking long-range order in iridium oxide by alkali ion for efficient water oxidation. *J. Am. Chem. Soc.* **141**, 3014–3023 (2019).
16. Hunter, B. M., Gray, H. B. & Müller, A. M. Earth-abundant heterogeneous water oxidation catalysts. *Chem. Rev.* **116**, 14120–14136 (2016).
17. Zhang, B. et al. Homogeneously dispersed multimetal oxygen-evolving catalysts. *Science* **352**, 333–337 (2016).
18. Hwang, J. et al. Perovskites in catalysis and electrocatalysis. *Science* **358**, 751–756 (2017).
19. Holger, D. et al. The mechanism of water oxidation: from electrolysis via homogeneous to biological catalysis. *ChemCatChem* **2**, 724–761 (2010).
20. Nellist, M. R., Laskowski, F. A. L., Lin, F., Mills, T. J. & Boettcher, S. W. Semiconductor–electrocatalyst interfaces: theory, experiment, and applications in photoelectrochemical water splitting. *Acc. Chem. Res.* **49**, 733–740 (2016).
21. Grimaud, A. et al. Activation of surface oxygen sites on an iridium-based model catalyst for the oxygen evolution reaction. *Nat. Energy* **2**, 16189 (2016).
22. Huang, Z. et al. Chemical and structural origin of lattice oxygen oxidation in Co–Zn oxyhydroxide oxygen evolution electrocatalysts. *Nat. Energy* **4**, 329–338 (2019).
23. Grimaud, A. et al. Activating lattice oxygen redox reactions in metal oxides to catalyse oxygen evolution. *Nat. Chem.* **9**, 457–465 (2017).
24. Roy, C. et al. Impact of nanoparticle size and lattice oxygen on water oxidation on $NiFeO_xH_y$. *Nat. Catal.* **1**, 820–829 (2018).
25. Yu, L. et al. Cu nanowires shelled with NiFe layered double hydroxide nanosheets as bifunctional electrocatalysts for overall water splitting. *Energy Environ. Sci.* **10**, 1820–1827 (2017).
26. Long, X., Wang, Z., Xiao, S., An, Y. & Yang, S. Transition metal based layered double hydroxides tailored for energy conversion and storage. *Mater. Today* **19**, 213–226 (2016).
27. Zhou, Y. et al. Exceptional performance of hierarchical Ni–Fe (hydr)oxide@ NiCu electrocatalysts for water splitting. *Adv. Mater.* **31**, 1806769 (2019).
28. Qiu, Z., Tai, C.-W., Niklasson, G. A. & Edvinsson, T. Direct observation of active catalyst surface phases and the effect of dynamic self-optimization in NiFe-layered double hydroxides for alkaline water splitting. *Energy Environ. Sci.* **12**, 572–581 (2019).
29. Yu, J., Wang, Q., O'Hare, D. & Sun, L. Preparation of two dimensional layered double hydroxide nanosheets and their applications. *Chem. Soc. Rev.* **46**, 5950–5974 (2017).
30. Liu, Z. et al. Synthesis, anion exchange, and delamination of Co–Al layered double hydroxide: assembly of the exfoliated nanosheet/polyanion composite films and magneto-optical studies. *J. Am. Chem. Soc.* **128**, 4872–4880 (2006).
31. Gao, S. et al. Ultrahigh energy density realized by a single-layer β-$Co(OH)_2$ all-solid-state asymmetric supercapacitor. *Angew. Chem. Int. Ed.* **53**, 12789–12793 (2014).
32. Ida, S., Shiga, D., Koinuma, M. & Matsumoto, Y. Synthesis of hexagonal nickel hydroxide nanosheets by exfoliation of layered nickel hydroxide intercalated with dodecyl sulfate ions. *J. Am. Chem. Soc.* **130**, 14038–14039 (2008).
33. Jin, H. et al. Emerging two-dimensional nanomaterials for electrocatalysis. *Chem. Rev.* **118**, 6337–6408 (2018).
34. Zhao, Y. F. et al. Sub-3 nm ultrafine monolayer layered double hydroxide nanosheets for electrochemical water oxidation. *Adv. Energy Mater.* **8**, 1703585 (2018).
35. Shao, Y. et al. Design and mechanisms of asymmetric supercapacitors. *Chem. Rev.* **118**, 9233–9280 (2018).
36. Su, X. Z. et al. Operando spectroscopic identification of active sites in NiFe Prussian blue analogues as electrocatalysts: activation of oxygen atoms for oxygen evolution reaction. *J. Am. Chem. Soc.* **140**, 11286–11292 (2018).
37. Zhao, S. et al. Ultrathin metal–organic framework nanosheets for electrocatalytic oxygen evolution. *Nat. Energy* **1**, 16184 (2016).
38. Capehart, T. W., Corrigan, D. A., Conell, R. S., Pandya, K. I. & Hoffman, R. W. In situ extended X-ray absorption fine structure spectroscopy of thin-film nickel hydroxide electrodes. *Appl. Phys. Lett.* **58**, 865–867 (1991).
39. Zheng, X. et al. Theory-driven design of high-valence metal sites for water oxidation confirmed using in situ soft X-ray absorption. *Nat. Chem.* **10**, 149–154 (2017).
40. Fabbri, E. et al. Dynamic surface self-reconstruction is the key of highly active perovskite nano-electrocatalysts for water splitting. *Nat. Mater.* **16**, 925–931 (2017).
41. Gong, M. et al. An advanced Ni–Fe layered double hydroxide electrocatalyst for water oxidation. *J. Am. Chem. Soc.* **135**, 8452–8455 (2013).
42. Song, F. & Hu, X. Exfoliation of layered double hydroxides for enhanced oxygen evolution catalysis. *Nat. Commun.* **5**, 4477 (2014).
43. Fei, H. et al. General synthesis and definitive structural identification of Mn_4C_4 single-atom catalysts with tunable electrocatalytic activities. *Nat. Catal.* **1**, 63–72 (2018).
44. Fan, K. et al. Nickel–vanadium monolayer double hydroxide for efficient electrochemical water oxidation. *Nat. Commun.* **7**, 11981 (2016).
45. Nørskov, J. K. et al. Origin of the overpotential for oxygen reduction at a fuel-cell cathode. *J. Phys. Chem. B* **108**, 17886–17892 (2004).
46. Li, Y.-F. & Selloni, A. Mechanism and activity of water oxidation on selected surfaces of pure and Fe-doped NiO_x. *ACS Catal.* **4**, 1148–1153 (2014).
47. Friebel, D. et al. Identification of highly active Fe sites in (Ni,Fe)OOH for electrocatalytic water splitting. *J. Am. Chem. Soc.* **137**, 1305–1313 (2015).
48. Seitz, L. C. et al. A highly active and stable IrO_x/$SrIrO_3$ catalyst for the oxygen evolution reaction. *Science* **353**, 1011–1014 (2016).
49. McCrory, C. C. L. et al. Benchmarking hydrogen evolving reaction and oxygen evolving reaction electrocatalysts for solar water splitting devices. *J. Am. Chem. Soc.* **137**, 4347–4357 (2015).
50. Ichiyanagi, Y. et al. X-ray absorption fine-structure study on the $Ni(OH)_2$ monolayer nanoclusters. *Chem. Phys. Lett.* **379**, 345–350 (2003).
51. Kresse, G. & Furthmüller, J. Efficiency of ab-initio total energy calculations for metals and semiconductors using a plane-wave basis set. *Comput. Mater. Sci.* **6**, 15–50 (1996).
52. Chen, J., Wu, X. & Selloni, A. Electronic structure and bonding properties of cobalt oxide in the spinel structure. *Phys. Rev. B* **83**, 245204 (2011).
53. Tkalych, A. J., Zhuang, H. L. L. & Carter, E. A. A density functional + U assessment of oxygen evolution reaction mechanisms on β-NiOOH. *ACS Catal.* **7**, 5329–5339 (2017).
54. Klimeš, J., Bowler, D. R. & Michaelides, A. Van der Waals density functionals applied to solids. *Phys. Rev. B* **83**, 195131 (2011).

Acknowledgements

The work performed at Beihang University was supported by the National Natural Science Foundation of China (51532001, 11974037, U1930402 and 52002010), the Beijing Natural Science Foundation (2194077) and the National Postdoctoral Program for Innovative Talents (BX20180020). We thank S. Zhang of the Shanghai Institute of Applied Physics for providing the standard XAFS data, and J. Zhang and L. Zheng of Beijing Synchrotron Radiation Facility for help with the in situ XAFS tests. We acknowledge the support of the NSRL (Beamlines MCD-A and MCD-B, Soochow Beamline for Energy Materials) in the XAS experiments. The computer resources of Tianhe-2 and Beihang HPC are both acknowledged.

Author contributions

J.K., L.-M.L. and L.G. designed and directed the study. J.K. and X.Q. conceived and performed the fabrications. Q.H. and L.-M.L. performed the first-principles calculations and analysed the results. X.G. and R.H. performed the spherical aberration-corrected TEM analyses. J.K., X.Q. and J.Z. participated in the characterization studies. All authors contributed to the discussions. J.K., Q.H., J.Z., C.W., L.L., X.D. and L.G. analysed the data and wrote the manuscript. All authors reviewed the paper.

Competing interests
The authors declare no competing interests.

Additional information
Supplementary information The online version contains supplementary material available at https://doi.org/10.1038/s41929-021-00715-w.

Correspondence and requests for materials should be addressed to Li-Min Liu or Lin Guo.

Peer review information *Nature Catalysis* thanks Hong-Jie Peng and the other, anonymous, reviewer(s) for their contribution to the peer review of this work.